Chemical Engineering Journal 480 (2024) 147499

Contents lists available at ScienceDirect

Chemical Engineering Journal

journal homepage: www.elsevier.com/locate/cej

ZnO Precursor's ability to catalyze formation of reactive oxygen species to degrade aqueous organic pollutants

Zoe A. Pollard [a], Madeline Karod [a], Alexa Schmitz [a], Brooke Pian [a], Buz Barstow [a], Jillian L. Goldfarb [a,b,*]

[a] Department of Biological and Environmental Engineering, Riley Robb Building, 111 Wing Drive, Cornell University, Ithaca, NY 14853, USA
[b] Smith School of Chemical and Biomolecular Engineering, Cornell University, Olin Hall, 113 Ho Plaza, Ithaca, NY, 14853, USA

ARTICLE INFO

Keywords:
Photocatalyst
Advanced oxidative process
Reactive oxygen species
Drinking water treatment
Chemiluminescence assay
Superoxide

ABSTRACT

Advanced oxidative processes (AOP) could mitigate emerging and persistent pollutants in drinking water. Yet there is a dearth of economical materials to generate the reactive oxygen species (ROS) that are responsible for pollutant degradation in AOPs. In this work, we design a zinc hydroxychloride monohydrate (ZHCM) silicon dioxide photocatalytic nanocomposite to generate ROS for non-selective degradation of drinking water contaminants. ZHCM is an intermediate phase in the sol–gel synthesis of ZnO-SiO_2-Ag nanocomposites containing 63–100 % ZnO. Typically, ZHCM is calcinated around 500 °C to crystallize into ZnO, yet we find that this calcination step may decrease photocatalytic activity. ZHCM exhibited higher methylene blue degradation efficiency through both catalysis (31 % after 4 h) and photocatalysis (98 % after 4 h) compared to the ZnO composites (~0% and 78 % after 4 h). ZHCM had the highest photodegradation efficiency for ciprofloxacin and caffeine. The increased catalytic and photocatalytic activity of these model pollutants is attributed to the generation of two ROS: superoxide anions in UV light and peroxide anions in the absence of light. These ROS were identified using a new modified biological assay measuring the chemiluminescence of luminol in the presence of horseradish peroxidase. Results are further verified via scavenger quenching tests. The ZHCM and ZnO-SiO_2-Ag are characterized for their antimicrobial activity measured by *E. coli* growth inhibition zones, band gaps, crystalline domains, and surface areas. This work demonstrates the potential to synthesize, at lower temperatures, a photocatalyst with enhanced ROS generation and reduced UV dependency.

1. Introduction

Emerging and persistent pollutants are detected in municipal water systems and natural waters alike [1]. Pharmaceuticals, such as antibiotics, are of particular concern due to their ecological, environmental, and human health hazards [2–7]. Dusi *et al.* identified over 600 active pharmaceutical compounds in natural waters [8]. Yet such emerging contaminants and persistent organic pollutants are not directly addressed in current drinking water treatment infrastructure; coagulation, flocculation, sedimentation, biological treatment, and ion exchange are ineffective for removal of many of these contaminants [3].

Advanced oxidative processes (AOPs) are a promising technology for non-targeted contaminant degradation in polluted waters. AOPs like photocatalysis generate reactive oxygen species (ROS, such as •OH radicals, peroxides, and superoxides) *in situ* to eliminate organic contaminants without chemical additives (e.g. chlorine, peroxides, or ozone) using UV or visible light often already existing in water treatment processes [14]. ROS promote demethylation and hydroxylation reactions wherein an organic compound is oxidized in successive steps into base components [15,16]. ROS degradation is non-targeted, and the reaction rates are relatively high (~10^9 M^{-1} s^{-1} for many pharmaceutical compounds [17]). Non-targeted techniques are well suited to treat water contaminated by a diverse mixture of pollutants that are present at low concentrations [18].

Abbreviations: AOP, advanced oxidative process; EDTA, ethylenediaminetetraacetic; HRP, horseradish peroxidase; ICP-MS, inductively coupled plasma-mass spectrometry; IPA, isopropanol; LB, Luria Bertani; MB, methylene blue; ROS, reactive oxygen species; TGA, thermogravimetric analysis; ZHCM, zinc hydroxychloride monohydrate.

* Corresponding author at: Department of Biological and Environmental Engineering, Riley Robb Building, 111 Wing Drive, Cornell University, Ithaca, NY 14853, USA.
E-mail address: Goldfarb@Cornell.edu (J.L. Goldfarb).

https://doi.org/10.1016/j.cej.2023.147499
Received 2 August 2023; Received in revised form 2 November 2023; Accepted 16 November 2023
Available online 24 November 2023

The photocatalytic properties of semiconductor metal oxides like ZnO are widely touted for their potential to remediate organic compounds in drinking water [1,19–21]. The efficiency and applicability of ZnO is limited by (1) a tendency to agglomerate, which reduces the effective surface area; (2) a narrow spectral range limiting the range of wavelengths available to activate the photocatalysts and (3) synthesis procedures that often require high temperature calcination steps, reducing the "greenness" of the materials synthesis process. The tendency to agglomerate [22–25] limits the already low surface area (10–20 m^2/g) of ZnO [26]. Embedding ZnO on catalyst carriers, including oxides like SiO_2 [22,27], activated carbons [28], and clays [29], can provide a structural scaffold to prevent particle clumping [24] and increase the photocatalyst's surface area and stability [30]. ZnO has a relatively narrow spectral absorption range ($\lambda < 400$ nm). If the absorption edge is broadened, the photocatalyst can be activated by a range of wavelengths in the ultraviolet (200 nm $< \lambda <$ 400 nm) and visible light (400 nm $< \lambda <$ 700 nm) regions. Adding a dopant, such as silver, can increase the spectral range to the near visible region and generate additional ROS species for contaminant degradation [31–33]. Finally, high temperature calcination increases the energy burden of ZnO photocatalyst synthesis. However, exisiting literature suggests that zinc hydroxychloride monohydrate (ZHCM, $Zn_5(OH)_8Cl_2{\cdot}H_2O$), a common intermediate compound in ZnO synthesis, may itself have photocatalytic activity.

ZHCM can be thermally converted into crystalline ZnO through hydrolysis [34] and vaporization reactions [35–37]. ZHCM is not only a precursor to the photocatalyst ZnO; several studies report potential photocatalytic activity of ZHCM to degrade aqueous pollutants. For example, Nekouei *et al.* [38] synthesized ZHCM and thermally converted it to ZnO, though they reported higher degradation by the ZnO than the precursor. A complex of ZHCM with ZnO was investigated previously for photocatalytic activity; Silva *et al.* [39] report limited photocatalytic activity by the composite and ZHCM precursor. The present work aims to address the limited photocatalytic activity of ZHCM seen in prior literature by reducing issues associated with agglomeration and by broadening the spectral range. This work presents the synthesis and characterization of a nanocomposite with both catalytic and photocatalytic activity not previously observed in ZHCM compounds. To the best of our knowledge, only one prior paper observed photocatalytic effect of N-doped ZHCM; while they observe significant adsorption in the absence of UV light, no catalysis is reported or mechanisms explored [40]. In contrast, we present an unmodified ZHCM synthesized without calcination. This work therefore highlights a green chemistry approach to catalysis in that the process does not require additional dopants nor high temperature calcination, reducing the heat and energy requirements of the synthesis.

In this work, we use a one-pot sol–gel process to synthesize a ZHCM-SiO_2-Ag nanocomposite which can be thermally converted into a ZnO-Ag-SiO_2 photocatalyst. In this paper, both nanocomposites are evaluated for their photocatalytic and catalytic potential to degrade three model compounds representing three different emerging contaminant classes: methylene blue dye [41] (industrial dye), ciprofloxacin [4,42] (antibiotic), and caffeine [4] (stimulant) to determine the potential for the ZHCM precursor to serve as an AOP photocatalyst, rather than its higher-energy requiring calcined form. Antibiotics are heavily used in agricultural practices and are prone to run-off into natural waters [9–11]. Stimulants like caffeine are found in natural waters such as the Hudson River Estuary [12]. Industrial dyes are widely produced and pose risks to human health and the environment [13]. The compounds used for these classes of contaminants were chosen for their previous use in literature and wide availability. The nanocomposites are characterized by XRD, band gap calculations, and antimicrobial activity. The photocatalytic activity is quantified by identifying reactive oxygen species through established scavenger experiments and a new application of a biological chemiluminescence method to AOP for water treatment.

2. Materials and methods

A one-pot sol–gel method was used to synthesize ZHCM, which is subsequently calcined into ZnO-SiO_2-Ag. The materials are characterized to determine band gap, crystalline domains, BET surface area, and antibacterial properties. The potential of these photocatalysts for degradation of emerging and persistent pollutants from drinking water is investigated and potential ROS production discussed.

2.1. Nanocomposite synthesis

4.34 mg zinc chloride (purity > 98.5, ACROS organics) was dissolved in 250. mL of 4:1 ethanol to Milli-Q water (18.2 MΩ cm^{-1}) mixture with a magnetic stir bar at 40 °C. To this, 10. mL of 2.0 N NaOH (VWR International) containing 2.94 mg of sodium metasilicate (anhydrous, purity > 95 %, STREM chemicals, inc.) was added dropwise at a rate of 2 mL min^{-1} while stirring. Immediately a white precipitate was observed at pH 6. The pH was adjusted to 9 with NaOH and the temperature increased to 90 °C for 15 min. The sample was cooled at room temperature for 4.5 h to crystallize it. For the silver containing nanocomposite, 65.15 mg silver nitrate (ACS grade, Sigma-Aldrich), weighed on a Shimadzu semi-microbalance to 0.01 mg, was added during the dissolution of the zinc chloride. Additionally, 2.49 mg sodium citrate dihydrate (ACS grade, Macron Fine Chemicals) was added during the 90 °C heating phase to reduce the silver. Free salts were removed from the nanocomposite by washing in 500 mL Milli-Q water then 100 mL ethanol via vacuum filtration. The material was dried overnight at ambient conditions (~12 h at 21 °C) in a fume hood. Half of the sample was retained as the uncalcined zinc hydroxychloride monohydrate (ZHCM) sample. The remaining nanocomposite was calcined to remove volatile compounds and thermally convert the ZHCM into ZnO. Calcination was performed in a ThermCraft Tube furnace under 100 mL/min dry air flowing at 500 °C for 1 h in a quartz boat. The cooled samples were stored in a desiccator at room temperature. A graphical representation of this synthesis is available in the Supplemental Information (SI, Figure S1).

2.2. Photocatalytic nanocomposite characterization

UV–Vis diffuse reflectance spectra (UV–Vis DRS) of the nanocomposites were recorded using a Cary 5000 UV–Vis-NIR Spectrophotometer equipped with a 150 mm integrating sphere assembly and the Small Spot Kit. Band gaps were calculated using the modified Kubuelka-Munk method [43,44] and the Urbach tail method was used to baseline the data [45,46].

Crystalline phases and mean crystallite diameter, $\langle d \rangle$, were determined using a Bruker D8Advance ECO powder diffractometer (XRD) with a Cu K-alpha x-ray source for a 2θ range of 20° to 80° at room temperature. Diffraction patterns were analyzed using the included Jade software package and compared to databases from the International Center for Diffraction Data. Miller indices were identified from the reference ZnO and Simonkolleite spectra. The mean crystallite diameter, $\langle d \rangle$, was estimated using the Scherrer equation [47,48].

Silver bonding determinations were measured on a Shimadzu Inductively Coupled Plasma Mass Spectrometry (ICP-MS-2030). 3.50 mg of nanocomposite was added to 10.0 mL of 70 % trace metal grade nitric acid (H_2NO_3, Fisher Scientific) in a 50 mL Teflon sealed digestion vial and digested in a CEM Corporation MARS 5 Digestion Microwave System. The sample was heated to 215 °C at a pressure of 800 psi with 900–1050 W of power and held for 15 min. After digestion, the supernatant was extracted, syringe filtered, and diluted to 2 % H_2NO_3 with Milli-Q water prior to ICP-MS analysis. The ICP-MS was calibrated for Zn (atomic mass 64) and Ag (atomic mass 109) with a 5-point calibration curve. The tuning solution, calibration solution, and internal standard were all purchased from High Purity Standards (USA). The mean weight fractions of ZnO, Ag, and SiO_2 were calculated from triplicate digestions

and ICP-MS analysis.

Thermogravimetric Analysis (TGA) describes the thermal stability, degree of calcination and surface adsorbed water for each nanocomposite. Using a TA Instruments TGA 5500 with 5 mg sample in platinum pans, the sample was heated to 500 °C at a rate of 10 °C min^{-1} under dry air with a flow rate of 25 mL min^{-1}. Measurements were conducted in duplicate, and the average percent mass loss reported.

Surface areas were measured via N_2 physisorption at 77 K over a P/P_0 range of 0 to 0.7 on a Micromeritics 3-Flex using the Brunauer–Emmett–Teller (BET) method after being degassed for 24 h at 130 °C on a Micromeritics Smart VacPrep. Measurements were conducted in triplicate with mean values and one standard deviation about the mean reported.

2.3. Antimicrobial properties of the nanocomposite

The nanocomposites were evaluated for their antibacterial activity against *Escherichia coli* (strain DH5α) using an agar disk diffusion assay. Luria Bertani (LB) agar plates were prepared, sterilized, and solidified. After solidification, each plate was inoculated with 1.0 mL of *E. coli* culture at 1.0 x 10^{-4} optical density (OD_{600}) in LB broth, swirled to coat evenly, and dried by a flame to prepare the bacterial lawn. The *E. coli* was prepared from a single colony in LB and allowed to grow at 37 °C for 12 h. The culture was diluted with LB to an OD_{600} of 0.1, incubated for 1 h to reach log phase and diluted to OD_{600} of 10^{-6} in LB. Nanocomposites were dispersed in water (sonicated for 30 min to create a stable colloid) at a concentration of 25 mg mL^{-1}. 30 μL was pipetted onto a sterile filter paper disk (Whatman 2017–006 Antibiotic Assay Paper, 1 cm disks) dried in an oven at 75 °C and repeated 4 times for a total loading of 3.0 mg of nanocomposite per disk. Loaded disks were aseptically placed on the dried inoculated agar plates and incubated inverted for 24 h at 37 °C. A negative and positive control were established using blank disks and disks loaded with kanamycin sulfate [49], respectively. Inhibition zones were observed around each sample and their diameters measured in millimeters (mm). Inhibition zones were repeated in triplicate and the averages and standard deviations are reported.

2.4. Degradation of model contaminants

Methylene blue (MB, 10 mg L^{-1}), ciprofloxacin (100 mg L^{-1}), and caffeine (100 mg L^{-1}) were used as model contaminants for the degradation studies (Table 1). The authors acknowledge that real-world water samples are likely more heterogenous; here we use individual model compounds as a proof of concept for the ZHCM as a photocatalyst and the demonstrate of a new biological assay for ROS species determination. Additional degradation conditions are discussed in SI Appendix 2. Degradations were conducted with *in situ* measurements in a 96-well plate (polystyrene, flat bottom) and concentrations monitored using a SynergyTM HT Multi-Mode Microplate Reader. Initial concentrations for the contaminants were determined based on the detection limit of the plate reader at the wavelengths provided in Table 1. 0.2 mg of the nanocomposite was weighed into a well using a Sartorius microbalance, after which 200 μL of the contaminant solution was pipetted into the well. The samples equilibrated for 20 min before illumination under the UV light at 10 cm. The UV light at 365 nm was supplied by an Analytik Jena 20-Watt UV bench lamp. The plate was transferred to the plate reader at each time point for absorption measurements at the characteristic wavelengths (Table 1) and then returned to the UV light for a total irradiation time of 4 h. Notably, this *in situ* measurement technique is beneficial in that the reaction conditions remain constant as no volume is extracted for measurement. All degradations were run in triplicate and conducted without any nanocomposite present as a control.

To determine the effects of vessel volume on the degradation kinetics, the degradation experiments for MB (10 mg L^{-1}) were repeated at 3 additional volumes in scintillation vials: 3-mL (1 dram), 6-mL (2 dram), and 40-mL (11 dram). The nanocomposite to volume ratio was preserved at each volume. At 3-mL, aliquots were analyzed on the plate reader using the described method. A Shimadzu UV–Vis Spectrometer was used to determine the MB concentration for 6-mL and 40-mL experiments using quartz cuvettes. Calibration curves for the plate reader and UV–Vis are provided in Supplemental Information (SI) Figure S2. 3- and 6-mL experiments were run in triplicate, but due to limitations in available material the 40-mL experiment was only run once.

2.5. Identification of reactive oxygen species responsible for photocatalytic activity

The major ROS species responsible for the degradation of methylene blue were identified by including 1.0 mM of scavenger compounds in the 96-well plate degradation studies. Scavengers (which quench the reaction by selectively sequestering a particular ROS) used in this study were ethylenediaminetetraacetic acid [50–53] (EDTA, hole (h^+) scavenger), sodium chloride [7] (NaCl, h^+ and •OH scavenger), isopropanol [40,53] (IPA, •OH scavenger), and hydroquinone [54] (HQ, $\bullet O_2^-$ scavenger). Quenching experiments were conducted as described in Section 2.4; the scavengers were added to 1.0 mM when the 200 μL of solution was dispensed into each well. Quenching experiments were repeated in triplicate and the mean and standard deviation reported.

The intensity and nature of the ROS generated was further

Table 1
Model water contaminants used to assess photocatalytic activity.

Contaminant	Commercial Use	Molar Mass (g/mol)	UV Peak Wavelength (nm)	Structure
Methylene Blue(MB)	Dye	319.9	664	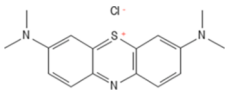
Ciprofloxacin	Antibiotic	367.8	300	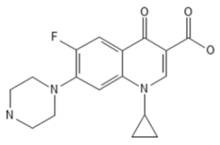
Caffeine	Stimulant	194.2	284	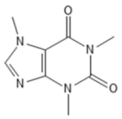

investigated using a modified biological assay that measures horseradish peroxidase catalyzed luminol excitation [55]. The levels as well as the duration of the chemiluminescence are proportional to the amount of ROS produced by the nanocomposite [56]. This is the first (to our knowledge) time such an assay was applied to study photocatalysts. Fig. 1 details the mechanism behind this biological assay. In the presence of the ROS generated by the photocatalyst, electrons in the luminol are excited. To return to the ground state, light is emitted and the luminol converted into aminophthalic acid. This emitted light is measured by the plate reader and can be used as a proxy for the measurement of the ROS. This luminol-derived chemiluminescence detects superoxide anions ($\bullet O_2^-$) without horseradish peroxidase (HRP) and detects both superoxide anions and peroxide radicals ($\bullet O_2^{2-}$) in the presence of HRP [55].

To prepare the chemical reagents, 15 mg luminol was dissolved into 1 mL liquid DMSO (dimethyl sulfoxide) and 5 mg HRP was dissolved in 500 µL of Milli-Q water. Reagents were divided into aliquots and stored in a −20 °C freezer until used. Immediately prior to the reaction an aliquot of luminol and HRP stock solutions were thawed at room temperature and two 5x solutions were prepared of 7.5 µL luminol stock in 1.5 mL Milli-Q water: one with 7.5 µL HRP stock added and the other with luminol only. The assay was carried out in 96 well plates with white sides and clear flat bottoms (Thermo Scientific™ Nunc MicroWell 96-Well Optical-Bottom Plates) with a uniform total volume per well of 100 µL across all samples. 0.5 mg of the nanocomposite was weighed into each well using a Sartorius microbalance. 80 µL of Milli-Q water was added to each well, and a baseline chemiluminescence measurement was recorded at a center wavelength of 460 nm with a bandpass of 40 nm using the same plate reader. Next, the entire plate was exposed to the UV lamp at 10 cm for 1 min. 20 µL of luminol solution (with or without the HRP) was quickly added using a multi-channel pipettor and transferred to the plate reader. After 5 s shaking at high intensity, the first chemiluminescence measurement was recorded. The time from the end of the UV light exposure to the first measurement was 15–20 s. 30 additional measurements were taken with a 3 sec shake between each measurement over the course of 20 min. Experiments were repeated with the UV light turned off but the same 1 min delay time to gauge the catalytic behavior in the absence of light.

3. Results and discussion

In this work, a ZHCM nanocomposite is developed for the degradation of organic drinking water contaminants. XRD confirmed the crystalline structure of the raw ZHCM precursor as zinc hydroxychloride monohydrate (ZHCM, $Zn_5(OH)_8Cl_2{\cdot}H_2O$) as shown in Fig. 2a.

The complete hydrolysis and oxidation of ZHCM into ZnO depends on experimental conditions (furnace dimensions, relative humidity, flow rate, temperature, pressure, and duration) [34,37]. XRD spectra in Fig. 2b confirms complete calcination due to the presence of only the nine representative ZnO peaks in the ZnO-SiO_2 sample. The inclusion of Ag in the crystalline phase is validated by the presence of one additional Ag (1 1 1) peak at $2\theta = 38°$ [22]. From the XRD, we see that SiO_2 is amorphous and does not alter the crystalline structure of the core material [57,58]. SiO_2 does not present as distinct peaks on the pattern (potential crystalline SiO_2 peaks would appear at $2\theta = 25°$, but no peaks were observed). The preferential crystal growth direction for our calcinated nanocomposites was (1 0 1) at $2\theta = 36°$, determined via the relative intensities of the characteristic ZnO peaks [59]. The nanocomposites were uniform in size with consistent XRD peak widths; silver-containing crystalline domains had a lower mean crystallite diameter than those without silver (Table 2).

As determined by ICPMS, the silver concentration in the ZnO-SiO_2-Ag nanocomposite was 4 % w/w (Table 2) which is consistent with the expected ratio based on the synthesis conditions. Nitric acid does not dissolve Si compounds implying that the Zn and Ag are not covalently bonded to the SiO_2. Literature values for the BET surface area of ZnO formed by the decomposition of mineralized simonkolleite [35] were significantly lower (1.3 $m^2\,g^{-1}$) than that achieved in this study (58.2 $m^2\,g^{-1}$; Table 2) which can be attributed to the inclusion of the porous SiO_2 scaffold phase. The nanocomposites exhibit micro- and *meso*-porosity. The synthesized ZHCM composite with the SiO_2 scaffold has lower surface area (18.9 $m^2\,g^{-1}$) than its natural mineral counterpart, simonkolleite, (27 $m^2\,g^{-1}$) due the presence of naturally occurring heterostructures [60].

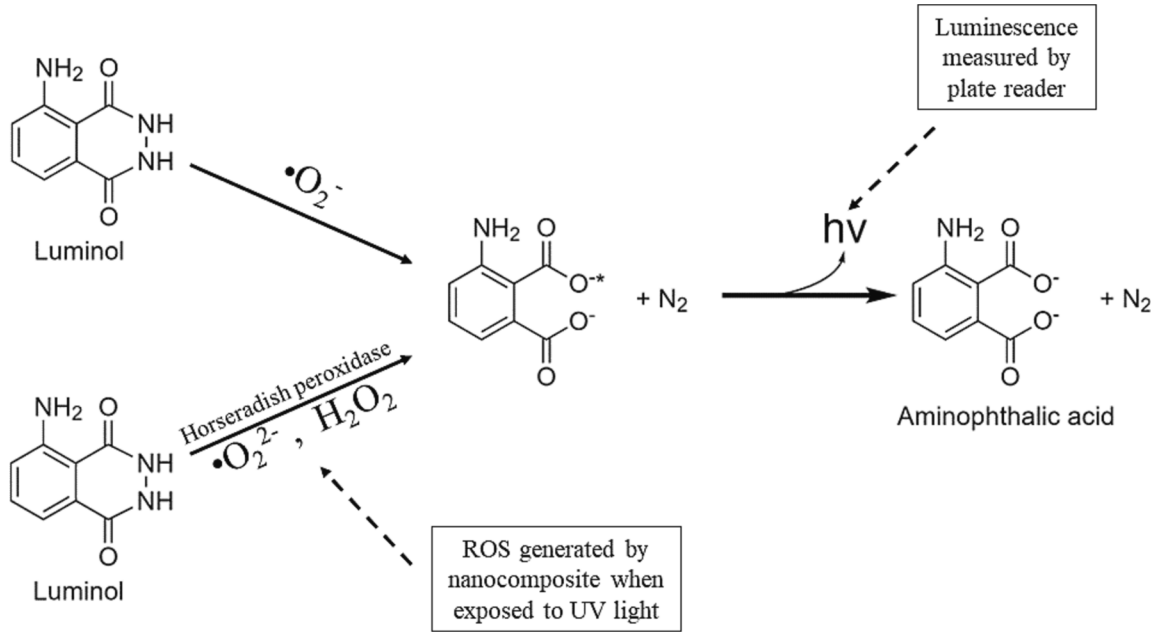

Fig. 1. Mechanism for the biological assay measuring chemiluminescence generated by luminol excited by the reactive oxygen species (ROS) generated by the photocatalytic nanocomposite. There are two pathways, in the presence of HRP, a combination of $\bullet O_2^-$ and $\bullet O_2^{-2}$ ROS excite the luminol, without HRP only $\bullet O_2^-$ excites the luminol.

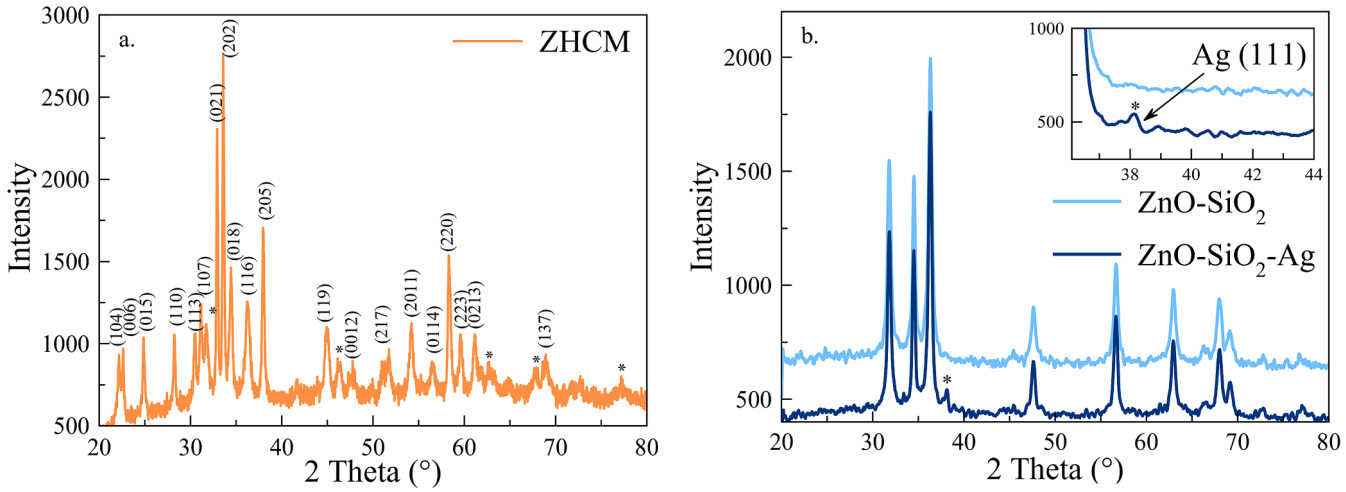

Fig. 2. XRD diffraction patterns for **a.** as-synthesized ZHCM **b.** calcined ZnO-SiO_2 sample and calcined ZnO-SiO_2-Ag sample. The inset in **b** zooms in on the Ag (1 1 1) peak.

Table 2
Photocatalytic nanocomposite properties. Component ratios (ZnO: SiO_2: Ag), mean crystallite diameter < d>, band gaps (direct allowed transition), inhibition zones (mm) (average ± one standard deviation), and BET surface area (m^2/g) (± standard deviation based on BET equation fit to partial pressure data).

Sample	Ratio (ZnO: SiO_2:Ag)	< d > (nm)	Band Gap (eV)	Inhibition Zone (cm)	BET Surface Area (m^2/g)
ZnO	100:0:0	41	3.20	1.60 ± 0.04	20.1 ± 0.1
ZnO-SiO_2	85:15:0	62	3.24	1.50 ± 0.05	58.2 ± 0.3
ZnO-SiO_2-Ag	63:33:4	35	3.21	1.50 ± 0.05	57.3 ± 0.7
ZHCM	–	–	3.32	1.46 ± 0.04	18.9 ± 0.2

3.1. Absorbance and bandgap

Diffuse reflectance UV–Vis spectra are shown in Fig. 3a. All materials exhibit the characteristic broad-spectrum absorbance of ZnO in the UV region (<400 nm), though silver did not produce a plasmon peak near 480 nm as had been reported previously [23]. However, there was a noticeable shift in the absorption maximum (especially nearing the visible range) for nanocomposites including Ag which is consistent with the literature [26]. Optical bandgaps (Table 2) are calculated from Tauc plots as an approximation for the electronic bandgaps [43]. Fig. 3b-e breaks down the possible transitions in Tauc plots for ZHCM (complete Tauc plots and further discussions are included in SI Figure S3 and S4). Calcination resulted in a slight decrease in the direct allowed transition confirming the appearance of confined carriers upon the formation of ZnO nanocrystals. ZnO nanocomposites exhibited a direct allowed transition with a band gap of 3.20 eV, and a second transition at ~ 3.1 eV but the nature of this second transition is unclear (direct forbidden, indirect allowed, or indirect forbidden) for all materials. The ZHCM has a direct allowed transition at 3.32 eV, with a second transition between

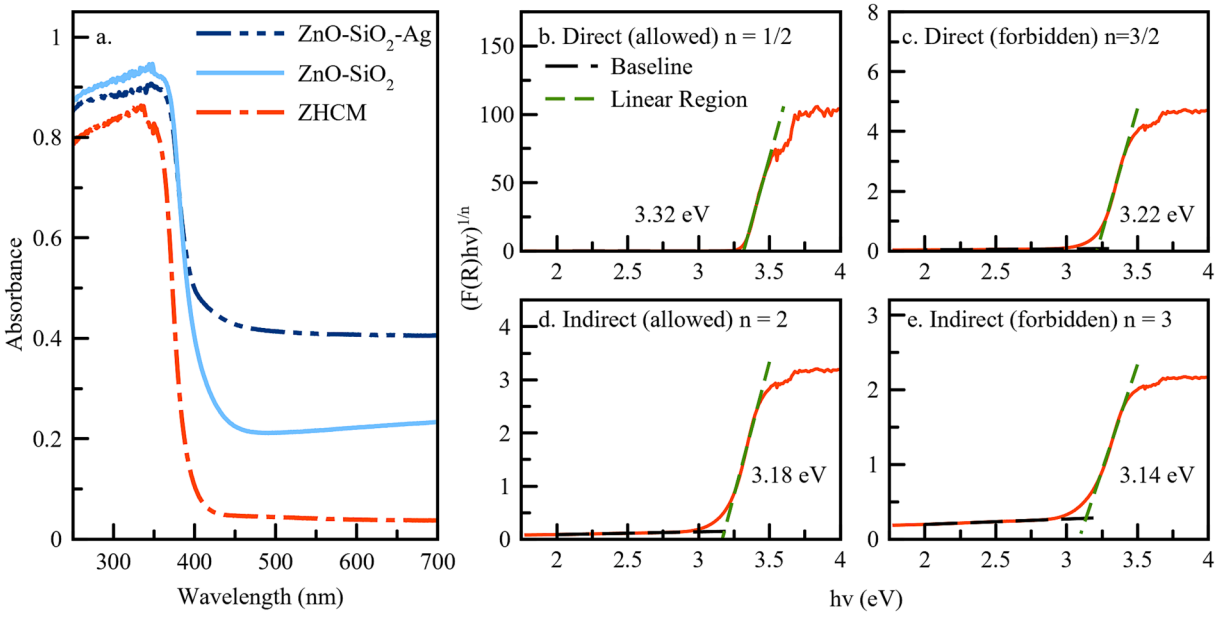

Fig. 3. UV–Vis analysis of nanocomposite including **a.** diffuse reflectance absorbance spectra and representative bandgap calculation for ZHCM nanocomposite using Tauc plots for **b.** direct allowed transitions, **c.** direct forbidden transitions, **d.** indirect allowed transitions, and **e.** indirect forbidden transitions.

3.14 and 3.22 eV. The band gap indicates that UV-light photons with energy of greater than or equal to 3.2 eV would excite an electron from the valence band to the conduction band. In an aqueous environment, these photogenerated holes and electrons react with water or surface hydroxides to form the ROS responsible for contaminant degradation. Additional descriptions of the ROS generated in this work and a schematic for ROS generation in aqueous environments is provided in SI Appendix 2 supported by Figure S10. Silver inclusion did not significantly shift the bandgap (as the differences reported in Table 2 are not significant within the sensitivity limits of the instrumentation) consistent with previous reports [50].

3.2. Inhibition of bacterial growth

While often overlooked in the design of AOP materials literature, the inhibition of bacterial growth could be a beneficial property for implementing these materials in water treatment applications. Zinc oxide composites inhibit bacterial growth by disorganizing bacterial cell membranes [61,62]. The presence of ZnO and Ag could prevent the attachment and colonization of bacteria and other microorganisms and reduce the formation of biofilms. Prior work found that ZnO nanoparticle size is inversely correlated with inhibition zone size [61]. In the case of our nanocomposite the particles were uniform and a decrease in crystallite domain was not correlated with any increase in inhibition zone (Table 2). The ZHCM exhibited a slightly narrower inhibition zone than the other nanocomposites. Pure ZnO had the widest inhibition zone by a small but statistically significant margin (p value = 0.002, two-tailed t-test) and the concentration of ZnO was not proportional to the decrease in inhibition (i.e., the inclusion of 15 or 33 % inert SiO_2 in the nanocomposite did not impact the degree of inhibition reduction). Under the same experimental conditions, the nanocomposites showed a comparable inhibition zone to 3.0 μg of kanamycin (1.49 ± 0.1 mm). Representative inhibition zones for each nanocomposite in the presence of kanamycin at 3.0 μg, 30 μg (3.13 ± 0.04 mm), and 150 μg (4.17 ± 0.05 mm) per disk are included in the Supplemental Information (SI Figure S5).

3.3. Determination of photocatalytic activity

Methylene blue (MB), ciprofloxacin, and caffeine were used as model contaminants to determine the photocatalytic activity of the nanocomposite. Each contaminant was degraded in the presence of UV light for 4 h, and for MB the degradation was repeated for three cycles to assess the reusability of the material (Fig. 4).

ZHCM completely degrades the methylene blue (efficiency 98 %) in 4 h; in the same amount of time the other photocatalysts tested achieved less than 80 % degradation. ZHCM also achieved the highest degradation efficiency for caffeine and ciprofloxacin. The degradations follow a pseudo-first-order kinetic model (kinetic parameters provided in Table 3 and linearized -ln(C_t/C_0) vs time plots provided in SI Figures S6-8). Reaction rates for ZHCM were 3-fold higher than the calcined ZnO composite for MB and 2-fold higher for ciprofloxacin and caffeine. Each catalyst tested in this work was also effective at initiating caffeine degradation. Without a catalyst under UV-light irradiation, the caffeine did not degrade to any measurable degree, suggesting that caffeine degradation is photocatalytically initiated.

The half-life ($t_{1/2}$) was calculated based on the pseudo-first order rate constant (Table 3). ZHCM-catalyzed degradation resulted in shorter $t_{1/2}$ compared to the other catalysts for each of the contaminants tested. Methylene blue degradation catalyzed by ZHCM had a $t_{1/2}$ of only 33 min compared to 283 and 810 min for ciprofloxacin and caffeine, respectively. The degradation efficiency, and consequently the $t_{1/2}$, is dependent on the catalyst, the contaminant moiety, and the ROS participating, as well as environmental factors (scavenger ions, pH, temperature, etc.) [63]. MB is often used for literature comparison as it readily degrades [64] and is easily detectable as the dye decolors due to hydroxylation and demethylation reactions [65,66]. Caffeine typically degrades less readily than MB [67] and involves pyrimidine ring opening reactions [68]. Additionally, ciprofloxacin is more resistent to ROS degradation than MB [71] as it degrades by quinolone ring opening

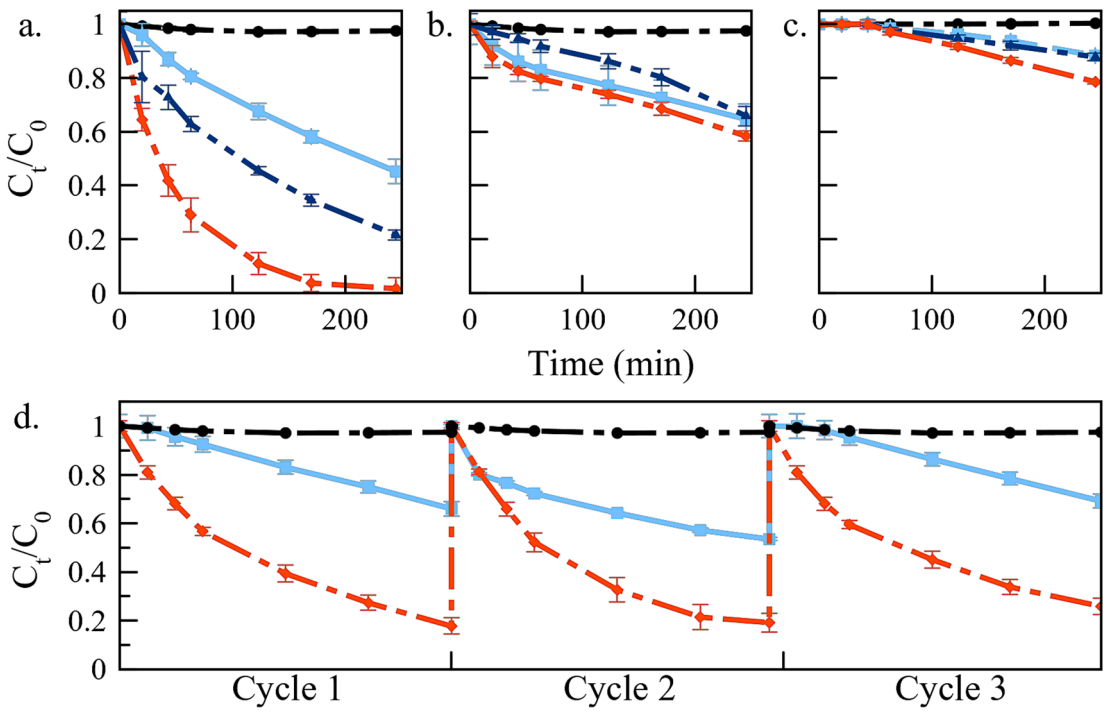

Fig. 4. Photocatalytic activity displayed as fraction of concentration remaining at any given time as a function of initial concentration (C_t/C_0) of ZHCM, ZnO-SiO_2, and ZnO-SiO_2-Ag including direct degradation of **a**. methylene blue (MB), **b.** ciprofloxacin, **c.** caffeine, and **d.** the repeatability for MB degradation. Error bars represent ± one standard deviation about the mean for 3 repeated trials. (For interpretation of the references to colour in this figure legend, the reader is referred to the web version of this article.)

Table 3
Kinetic parameters for the photocatalytic degradation of methylene blue, ciprofloxacin, and caffeine (Calculated from data shown in Fig. 4) including degradation efficiency after 240 min irradiation, pseudo first-order rate constant (k_1), adjusted R^2 values for the fit of the pseudo first-order model, and the compounds half-life ($t_{1/2}$) under the specified degradation conditions.

Contaminant	Sample	Degradation Efficiency (%)	$k_1 \times 10^{-3}$ (min^{-1})	R^2	$t_{1/2}$ (min)
Methylene Blue	No catalyst	10.0	0.350	0.932	1981
	ZnO-SiO_2	55.0	3.32	0.993	153
	ZnO-SiO_2-Ag	78.0	6.88	0.989	101
	ZHCM	98.0	21.0	0.999	33.0
Ciprofloxacin	No catalyst	14.0	0.410	0.805	1680
	ZnO-SiO_2	39.0	2.00	0.997	346
	ZnO-SiO_2-Ag	34.0	1.47	0.969	472
	ZHCM	42.0	2.45	0.941	283
Caffeine	No catalyst	0.00	0	–	–
	ZnO-SiO_2	12.0	0.420	0.942	1651
	ZnO-SiO_2-Ag	12.0	0.420	0.981	1651
	ZHCM	21.0	0.855	0.967	810

[69,70], a more energy-intensive process owing to the more stable aromatic molecules. Silver particles in the nanocomposite increased the conversion of MB as compared to the ZnO-SiO_2, but the effect of silver on the degradation of caffeine and ciprofloxacin was minimal. The degradation rate for each of the compounds was not correlated with the mean crystallite size, <d>, or particle size of the nanocomposite. Additional discussion of reactive oxygen species (ROS) generated and degradation pathways of the model compounds is discussed in Appendix 1 of SI.

Notably, high photocatalytic degradation efficiency can be achieved without the energy input of calcination where the nanocomposite is heated at 500 °C for ~ 1 h. A comparison of the photocatalytic degradation efficiencies achieved in this work with existing literature is provided in SI Table S1 (materials properties) and S2 (degradation efficiencies). Literature suggests that higher surface area is correlated with a higher degradation efficiency; this is often attributed to improved dispersion of catalytically active sites [38,72]. However, in this work we found that our raw ZHCM material has a significantly higher degradation potential for the compounds tested, while the bandgap and BET surface area are lower as compared to the multiphase ZnO-SiO_2-Ag nanocomposite. However, the literature trend correlating surface area and photocatalytic efficiency is often based on the same materials with different morphological properties. Our work suggests that surface area alone is not the driving force for catalytic activity, but perhaps accessibility of *more* catalytically active sites *and* the nature of the sites. The precipitate forming the ZHCM, while it has a lower surface area than the calcined ZnO, may have more accessible active sites for ROS generation, which would be supported by the higher bandgap achieved by this sample.

Negative slopes on Fig. 4 for photocatalyst-based experiments indicate that the reaction is still proceeding and has not yet reached completion or equilibrium. It is likely that if the reaction proceeded to completion or equilibration, error for the pseudo-first order fit would decrease as we deviate from the initial linear behavior of the degradation [18]. Additionally, the ZHCM nanocomposite is reusable over multiple cycles. Fig. 4d shows the results of repeated trials where additional methylene blue was added over three cycles. ZHCM maintained its efficiency over the course of this experiment while the ZnO-SiO_2 lost roughly 20 % of its degradation efficiency. Previous studies attribute this loss in activity to surface roughening and photocorrosion [73].

It has been shown that at a higher pH (nearing 11) surface absorbed water molecules can be reduced at the surface of the photocatalyst [74]. The pH of the 10 mg L^{-1} MB solution during degradation was 10.6. The redox potential of the surface $H_2O/•OH$ couple is 2.73 eV which is lower than the bandgap of the catalysts, resulting in more hydroxide ions reacting with photoexcited holes to generate additional ROS. TGA and derivative thermogravimetric (DTG) curves (Fig. 5) confirm a rapid mass loss for ZHCM of 7.3 % at 175 °C which is consistent with the loss of surface absorbed water [36]. Physically bound water is released below 120 °C and, due to the materials being stored in a desiccator, accounts for only 2.3 % of the mass loss. Above 200 °C the ZHCM intermediates are crystallized into ZnO, and volatiles (mainly HCl) are driven off via hydrolysis and devolatilization [37]. This surface absorbed water may explain the 2- to 3-fold increase in the photocatalytic ability of the ZHCM as compared to its calcinated ZnO forms. The mechanisms and exact stoichiometric mass loss for ZHCM thermal conversion to ZnO in this work do not perfectly align with literature values [37] due to the inclusion of SiO_2 in the matrix. Additionally, the ZnO-SiO_2 and ZnO-SiO_2-Ag were thermally stable with a total mass loss of less than 1.5 %, which occurred mostly below 120 °C.

3.4. Reactive oxygen species identification

MB degradation studies in the presence of four radical scavengers were used to identify the ROS responsible for the photocatalytic activity. Scavengers included EDTA (hole (h^+) scavenger), NaCl (h^+ and •OH scavenger), IPA (•OH scavenger), and HQ ($•O_2^-$ scavenger). NaCl is an ionic compound found ubiquitously in natural and treated waters alike and is used here to both understand ROS and as a representative inorganic environmental water. Co-existing chloride and sulfide ions in water will alter the ROS further, but their role is beyond the scope of this work, which focuses on model compounds and ROS species identification. By adding the scavenger, we see a decrease in the degradation efficiency as the scavengers selectively sequester the ROS (Fig. 6). HQ has the strongest inhibitory effect on the photocatalytic degradation, suggesting that superoxide ions are the primary species while holes and hydroxyl radicals play a secondary role. Silver in the nanocomposite acts

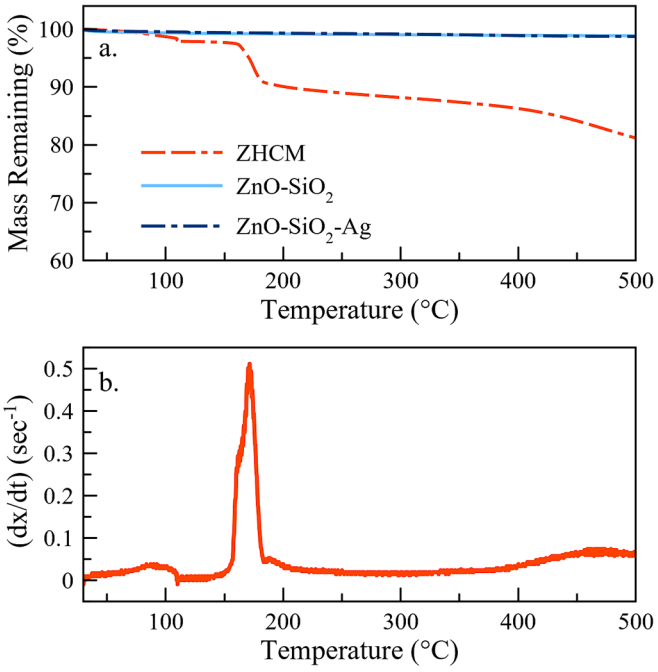

Fig. 5. a. TGA thermal analysis under air for ZHCM, ZnO-SiO_2, and ZnO-SiO_2-Ag, and b. DTG curve showing the thermal degradation of ZHCM into ZnO.

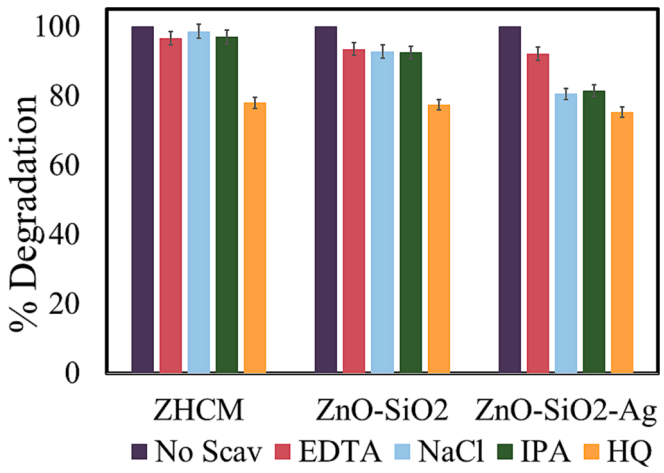

Fig. 6. The effect of scavenger quenching on methylene blue degradation for ZHCM, ZnO-SiO_2, and ZnO-SiO_2-Ag with ethylenediaminetetraacetic acid (EDTA), sodium chloride (NaCl), isopropyl alcohol (IPA), and hydroquinone (HQ). Error bars represent ± one standard deviation about the mean. (For interpretation of the references to colour in this figure legend, the reader is referred to the web version of this article.)

as an electron sink where absorbed oxygen may be reduced into various ROS species. The inclusion of silver appears to have diversified the ROS species generated as we see some inhibition with the inclusion of NaCl and IPA which both scavenge hydroxyl radicals.

Fig. 7 shows a higher measured luminol amplified chemiluminescence for the ZHCM as compared to the calcinated ZnO-SiO_2-Ag. Experiments were conducted in triplicate and while there was high variability, statistically significant differences were found by comparing ranges generated by one standard deviation about the mean. Luminol-amplified chemiluminescence can detect superoxide anions ($\bullet O_2^-$) without HRP and can detect both superoxide anions and peroxides ($\bullet O_2^{2-}$ and H_2O_2) in the presence of HRP [55]. For ZHCM the highest chemiluminescence was observed in the presence of luminol under UV light, which confirms a high superoxide anion concentration. This is in direct agreement with the quenching effect of HQ. No chemiluminescence was detected in the absence of light for the luminol only assay for either catalyst. This indicates that the generation of superoxide anions is light dependent. Peroxide radicals, on the other hand, were detected regardless of the UV light state and were comparable for the two photocatalysts tested with UV-light exposure. Interestingly, the ZHCM generated substantial peroxide radicals in the absence of light, which explains its catalytic potential in addition to its photocatalytic behavior [75].

To further probe the catalytic behavior, MB degradation studies were repeated in the absence of UV-light (data available in Figure S9). These results confirm catalytic activity for the ZHCM with a degradation efficiency of 31 % after 4 h. The degradation of MB in the absence of light can be attributed to a mix of adsorption and bond cleavage by the peroxide radicals generated by ZHCM. ZnO-SiO_2-Ag did not exhibit any catalytic effect in dark trials; this is consistent with the lack of any observed ROS generation without UV light exposure. Higher peroxide formation and lower dependence on UV-light activation may explain the higher overall photocatalytic degradation efficiency of the ZHCM compound compared to the ZnO composites. Neither adsorption nor catalytic behavior was exhibited by the ZnO composites in the absence of UV light.

The reaction involved in the biological assay is complex and a quantification of ROS is not feasible. However, the current assay indicates a correlation between higher ROS generation (by luminol chemiluminescence as a proxy) and the photodegradation of model contaminants. Future work is required to convert this biological assay (which is standardized for biological cell use) to a robust tool for determining ROS lifetimes and concentrations for AOP evaluation.

Overall, we observed higher degradation efficiencies for our ZHCM than the ZnO composites synthesized in this work. We report the physical properties and reusability of the nanocomposites and identify the reactive oxygen species responsible for the contaminant degradation. The ZHCM exhibits catalytic and photocatalytic behavior allowing for contaminant degradation with or without UV light application resulting in a more robust and flexible AOP.

4. Conclusions

This work identifies a ZHCM precursor with high photocatalytic and catalytic activity for the degradation of three model contaminants (methylene blue, caffeine, and ciprofloxacin). ZHCM within an SiO_2 scaffold is thermally converted into ZnO-SiO_2 nanocomposites (with and without Ag dopant). The ZHCM exhibits both catalytic and photocatalytic activity indicating the potential to degrade contaminants both in the presence of UV light and when no light is present. The ZHCM catalyst exhibited nearly 2x higher degradation than the ZnO photocatalyst for the degradation of methylene blue (98 %), caffeine (42 %), and ciprofloxacin (21 %).

A standard scavenger experiment was used to identify the ROS species responsible for the contaminant degradation and was expanded by a biological assay using horseradish peroxidase and luminol. For ZHCM, peroxides and superoxide ROS were identified as the primary species responsible for the degradation of methylene blue dye. In the absence of light, ZHCM generated peroxide radicals and achieved a degradation efficiency of 31 % for methylene blue. In the absence of light, the ZnO

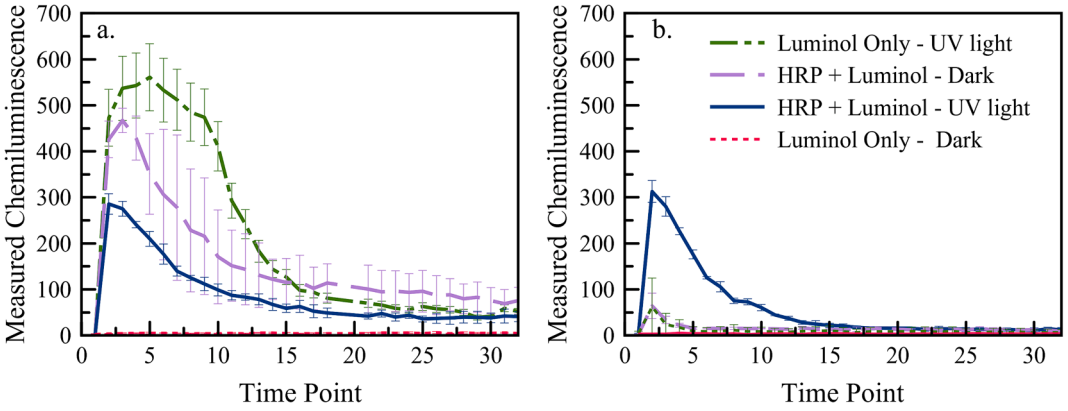

Fig. 7. Reactive oxygen species generation as measured by the chemiluminescence of luminol with or without HRP over repeated measurements for a. ZHCM and b. ZnO-SiO_2-Ag. Error bars represent ± one standard deviation about the mean for 3 repeated trials.

composites did not exhibit catalytic activity as measured by ROS detected by the luminol chemiluminescence assay and degradation experiments. The ZHCM exhibited high stability over repeated trials, while ZnO-SiO_2 composites lost nearly 20 % of its degradation efficiency after 3 cycles.

The ZHCM has a low BET surface area (18.9 m^2/g) and comparable bandgap to ZnO-SiO_2. As such, the increased photocatalytic performance can be attributed to more ROS generation and a higher ratio of surface absorbed water. Overall, the ZHCM has a higher photocatalytic and catalytic activity with a lower energy requirement than the ZnO-SiO_2-Ag produced in this work. While it is infeasible to test these newly developed catalysts in every environmental condition or contaminant mixture, this study demonstrates (1) the development of an effective catalyst/photocatalyst with a lower energy cost than the incumbent which is widespread in the literature (2) the potential of this material to act on three different classes of contaminants with various levels of persistence. These photocatalytic nanocomposites could be used in a tertiary treatment step in addition to traditional wastewater treatment for the removal of currently persistent pollutants. ZHCM catalysis and photocatalysis could provide nontargeted treatment for a broad range of contaminants using existing UV-light infrastructure in water treatment plants.

CRediT authorship contribution statement

Zoe A. Pollard: Conceptualization, Methodology, Investigation, Writing – original draft, Visualization. **Madeline Karod:** Conceptualization, Writing – review & editing. **Alexa Schmitz:** Conceptualization, Methodology, Investigation. **Brooke Pian:** Investigation. **Buz Barstow:** Writing – review & editing, Resources, Supervision. **Jillian L. Goldfarb:** Conceptualization, Methodology, Writing – original draft, Writing – review & editing, Resources, Funding acquisition, Supervision.

Declaration of competing interest

The authors declare the following financial interests/personal relationships which may be considered as potential competing interests: [Jillian L. Goldfarb reports financial support was provided by the US National Science Foundation].

Data availability

Data will be made available on request.

Acknowledgements

This work was supported by the National Science Foundation through CMMI grant 1727316. This work made use of the Cornell Center for Materials Research Shared Facilities which are supported through the NSF MRSEC program (DMR- 1719875).

Appendix A. Supplementary data

Supplementary data to this article can be found online at https://doi.org/10.1016/j.cej.2023.147499.

References

[1] C. Byrne, G. Subramanian, and S. C. Pillai, Recent Advances in Photocatalysis for Environmental Applications, (2017).
[2] R. Pulicharla, F. Proulx, S. Behmel, J.B. Sérodes, M.J. Rodriguez, Occurrence and seasonality of raw and drinking water contaminants of emerging interest in five water facilities, Sci. Total Environ. 751 (2021).
[3] C. Adams, Y. Wang, K. Loftin, M. Meyer, Removal of antibiotics from surface and distilled water in conventional water treatment processes, J. Environ. Eng. 128 (2002) 253.
[4] S. Ahmed, F.S.A. Khan, N.M. Mubarak, M. Khalid, Y.H. Tan, S.A. Mazari, R.R. Karri, E.C. Abdullah, Emerging pollutants and their removal using visible-light responsive photocatalysis – a comprehensive review, J. Environ. Chem. Eng. 9 (2021), 106643.
[5] N.J. Niemuth, R.D. Klaper, Emerging wastewater contaminant metformin causes intersex and reduced fecundity in fish, Chemosphere 135 (2015) 38.
[6] P. Valbonesi, M. Profita, I. Vasumini, E. Fabbri, Contaminants of emerging concern in drinking water: quality assessment by combining chemical and biological analysis, Sci. Total Environ. 758 (2021).
[7] A. Hassani, A. Khataee, S. Karaca, Photocatalytic degradation of ciprofloxacin by synthesized TiO2 nanoparticles on montmorillonite: effect of operation parameters and artificial neural network modeling, J. Mol. Catal. A Chem. 409 (2015) 149.
[8] E. Dusi, M. Rybicki, and D. Jungmann, The Database“ Pharmaceuticals in the Environment”-Update and New Analysis, Umweltbundesamt Chemicals., (2019).
[9] S. yi dan Zhou, D. Zhu, M. Giles, T. Daniell, R. Neilson, X. ru Yang, Does reduced usage of antibiotics in livestock production mitigate the spread of antibiotic resistance in soil, earthworm guts, and the phyllosphere? Environ. Int. 136 (2020), 105359.
[10] M. N. Alnajrani and O. A. Alsager, Removal of Antibiotics from Water by Polymer of Intrinsic Microporosity: Isotherms, Kinetics, Thermodynamics, and Adsorption Mechanism, Scientific Reports 2020 10:1 10, 1 (2020).
[11] J. Wu, J. Wang, Z. Li, S. Guo, K. Li, P. Xu, Y. S. Ok, D. L. Jones, and J. Zou, Antibiotics and Antibiotic Resistance Genes in Agricultural Soils: A Systematic Analysis, Https://Doi.Org/10.1080/10643389.2022.2094693 (2022).
[12] C.M.G. Carpenter, D.E. Helbling, Widespread micropollutant monitoring in the hudson river estuary reveals spatiotemporal micropollutant clusters and their sources, Environ. Sci. Tech. 52 (2018) 6187.
[13] S. Dutta, B. Gupta, S. K. Srivastava, and A. K. Gupta, Recent Advances on the Removal of Dyes from Wastewater Using Various Adsorbents: A Critical Review, Materials Advances.
[14] E. Wysowska, I. Wiewiórska, A. Kicińska, The impact of different stages of water treatment process on the number of selected bacteria, Water Resour. Ind. 26 (2021), 100167.
[15] J. Wu, H. Yu, W. Liu, C. Dong, M. Wu, C. Zhang, Enhanced degradation of organic pollutant by bimetallic catalysts decorated micromotor in advanced oxidation processes, J. Environ. Chem. Eng. 10 (2022), 107034.
[16] M.S. Hossain, M.Y.A. Mollah, M.A.B.H. Susan, M.M. Islam, Role of in situ electrogenerated reactive oxygen species towards degradation of organic dye in aqueous solution, Electrochim. Acta 344 (2020), 136146.
[17] W.R. Haag, C.C. David Yao, Rate constants for reaction of hydroxyl radicals with several drinking water contaminants, Environ. Sci. Tech. 26 (1992) 1005.
[18] G. Rytwo, A.L. Zelkind, Evaluation of kinetic pseudo-order in the photocatalytic degradation of ofloxacin, Catalysts 12 (2022) 24.
[19] J.T. Adeleke, T. Theivasanthi, M. Thiruppathi, M. Swaminathan, T. Akomolafe, A. B. Alabi, Photocatalytic degradation of methylene blue by ZnO/NiFe2O4 nanoparticles, Appl. Surf. Sci. 455 (2018) 195.
[20] A.A. Almehizia, M.A. Al-Omar, A.M. Naglah, M.A. Bhat, N.S. Al-Shakliah, Facile synthesis and characterization of ZnO nanoparticles for studying their biological activities and photocatalytic degradation properties toward methylene blue dye, Alex. Eng. J. 61 (2022) 2386.
[21] A.A. Shah, M.A. Bhatti, A. Tahira, A.D. Chandio, I.A. Channa, A.G. Sahito, E. Chalangar, M. Willander, O. Nur, Z.H. Ibupoto, Facile synthesis of copper doped ZnO nanorods for the efficient photo degradation of methylene blue and methyl orange, Ceram. Int. 46 (2020) 9997.
[22] M. Kokate, K. Garadkar, A. Gole, Zinc-oxide-silica-silver nanocomposite: unique one-pot synthesis and enhanced catalytic and anti-bacterial performance, J. Colloid Interface Sci. 483 (2016) 249.
[23] S. Bettini, R. Pagano, P. Semeraro, M. Ottolini, L. Salvatore, F. Marzo, N. Lovergine, G. Giancane, L. Valli, SiO2-Coated ZnO nanoflakes decorated with ag nanoparticles for photocatalytic water oxidation, Chem. A Eur. J. 25 (2019) 14123.
[24] L. Qomariyah, W. Widiyastuti, K. Kusdianto, T. Nurtono, D. Anggoro, and S. Winardi, Electrospray Synthesis and Photocatalytic Activities of ZnO-SiO 2 Composites Particles Electrospray Synthesis and Photocatalytic Activities of ZnO-SiO2 Composites Particles, (n.d.).
[25] D.K.L. Harijan, S. Gupta, S.K. Ben, A. Srivastava, J. Singh, V. Chandra, High photocatalytic efficiency of α-Fe2O3 - ZnO composite using solar energy for methylene blue degradation, Physica B Condens Matter 627 (2022), 413567.
[26] A. Barhoum, G. Van Assche, H. Rahier, M. Fleisch, S. Bals, M.-P. P. Delplancked, F. Leroux, and D. Bahnemann, Sol-Gel Hot Injection Synthesis of ZnO Nanoparticles into a Porous Silica Matrix and Reaction Mechanism, 119, 270 (2017).
[27] M.B. Mohamed, M.H. Abdel-Kader, A.A. Alhazime, Structural and optical properties of doped ZnO/SiO2 nanocomposite, Int. J. Appl. Ceram. Technol. 1 (2018).
[28] R.K. Liew, M.Y. Chong, O.U. Osazuwa, W.L. Nam, X.Y. Phang, M.H. Su, C.K. Cheng, C.T. Chong, S.S. Lam, Production of activated carbon as catalyst support by microwave pyrolysis of palm kernel shell: a comparative study of chemical versus physical activation, Res. Chem. Intermed. 44 (2018) 3849.
[29] M. Karod, A.H. Hubble, A.R. Maag, Z.A. Pollard, J.L. Goldfarb, Clay-catalyzed in situ pyrolysis of cherry pits for upgraded biofuels and heterogeneous adsorbents as recoverable by-products, Biomass Convers. Biorefin. 2022 (2022) 1.
[30] D. Ghime and P. Ghosh, Advanced Oxidation Processes: A Powerful Treatment Option for the Removal of Recalcitrant Organic Compounds, in Advanced Oxidation Processes - Applications, Trends, and Prospects (IntechOpen, 2020).
[31] L.P.P. Ha, T.H.T. Vinh, N.T.B. Thuy, C.M. Thi, P. Van Viet, Visible-light-driven photocatalysis of anisotropic silver nanoparticles decorated on ZnO nanorods: synthesis and characterizations, J. Environ. Chem. Eng. 9 (2021), 105103.
[32] C.C. Chen, X. Zhou, T. Ding, J. Zhang, S. Wang, J. Xu, J. Chen, J. Dai, C.C. Chen, Preparation and characterization of ZnO/SiO 2 /Ag nanoparticles as highly

sensitive substrates for surface-enhanced raman scattering, Mater. Lett. 165 (2016) 55.
[33] Y. Dong, S. Zhan, P. Wang, A facile synthesis of ag modified ZnO nanocrystals with enhanced photocatalytic activity, J. Wuhan Univ. Technol. Mater. Sci. Ed. 27 (2012) 615.
[34] M.S. Aida, M. Hjiri, N.H. Alonizan, B. Zarrad, A.H. Hammad, M.K. Al Zahrani, ZnO and simonkolleite nanocomposite synthesis via green chemistry using hibiscus flower extract, ECS J. Solid State Sci. Technol. 10 (2021), 123016.
[35] A. Moezzi, M. Cortie, A. McDonagh, Transformation of zinc hydroxide chloride monohydrate to crystalline zinc oxide, Dalton Trans. 45 (2016) 7385.
[36] H. Tanaka, A. Fujioka, Influence of thermal treatment on the structure and adsorption properties of layered zinc hydroxychloride, Mater. Res. Bull. 45 (2010) 46.
[37] T. Kozawa, A. Onda, K. Yanagisawa, A. Kishi, Y. Masuda, Effect of water vapor on the thermal decomposition process of zinc hydroxide chloride and crystal growth of zinc oxide, J. Solid State Chem. 184 (2011) 589.
[38] F. Nekouei, S. Nekouei, Comparative study of photocatalytic activities of Zn5(OH) 8Cl2·H2O and ZnO nanostructures in ciprofloxacin degradation: response surface methodology and kinetic studies, Sci. Total Environ. 601–602 (2017) 508.
[39] A.C.A. Silva, M.J.B. Silva, A.A. Rocha, M.P.C. Costa, J.Z. Marinho, N.O. Dantas, Synergistic effect of simonkolleite with zinc oxide: physico-chemical properties and cytotoxicity in breast cancer cells, Mater. Chem. Phys. 266 (2021), 124548.
[40] J. He, J. Hu, X. Mo, Q. Hao, Z. Fan, G. He, Y. Wang, W. Li, Q. He, Novel photocatalyst nitrogen-doped simonkolleite Zn5(OH)8Cl2·H2O with Vis-up-conversion photoluminescence and effective visible-light photocatalysis, Appl. Phys. A Mater. Sci. Process. 125 (2019) 1.
[41] S. Modi et al., Recent and Emerging Trends in Remediation of Methylene Blue Dye from Wastewater by Using Zinc Oxide Nanoparticles, Water 2022, Vol. 14, Page 1749 14, 1749 (2022).
[42] X. Rong, F. Qiu, Z. Jiang, J. Rong, J. Pan, T. Zhang, D. Yang, Preparation of ternary combined ZnO-Ag 2 O/Porous g-C 3 N 4 Composite Photocatalyst and enhanced visible-light photocatalytic activity for degradation of ciprofloxacin, Chem. Eng. Res. Des. 111 (2016) 253.
[43] Z. Chen and T. F. Jaramillo, The Use of UV-Visible Spectroscopy to Measure the Band Gap of a Semiconductor, (n.d.).
[44] P. Makuła, M. Pacia, W. Macyk, How To Correctly Determine the Band Gap Energy of Modified Semiconductor, Photocatalysts Based on UV−Vis Spectra (2018).
[45] and D. P. B. Brian D. Viezbicke, Shane Patel, Benjamin E. Davis, Evaluation of the Tauc Method for Optical Absorption Edge Determination: ZnO Thin Films as a Model System Rutgers, Basic Solid State Physics 60, 1789 (2011).
[46] Z. Mirzaeifard, Z. Shariatinia, M. Jourshabani, S.M. Rezaei Darvishi, ZnO photocatalyst revisited: effective photocatalytic degradation of emerging contaminants using S-doped ZnO nanoparticles under visible light radiation, Ind. Eng. Chem. Res. 59 (2020) 15894.
[47] U. Holzwarth, N. Gibson, The scherrer equation versus the “debye-scherrer equation”, Nat. Nanotechnol. 6 (2011) 534.
[48] A. Monshi, M.R. Foroughi, M.R. Monshi, Modified scherrer equation to estimate more accurately nano-crystallite size using XRD, World J. Nano Sci. Eng. 2 (2012) 154.
[49] R. Faraji, A. Parsa, B. Torabi, T. Withrow, Effects of kanamycin on the macromolecular composition of kanamycin sensitive escherichia coli dh5! strain, J. Exp. Microbiol. Immun. (JEMI) 9 (2006) 31.
[50] M. J. The photocatalytic reaction is initiated by the absorption of UV-light photons with energy equal or higher than the band-gap in ZnO, which results in the creation of photogenerated holes in its VB and electrons in its CB, and then CB- electrons of ZnO eas, M. J. Lima, D. L. Baptista, A. M. T. Silva, C. G. Silva, and J. L. Faria, Ag-Loaded ZnO Materials for Photocatalytic Water Treatment, Chemical Engineering Journal 318, 95 (2017).
[51] P. Gu, C. Zhang, Z. Sun, H. Zhang, Q. Zhou, S. Lin, J. Rong, M.R. Hoffmann, Enhanced photoreductive degradation of perfluorooctanesulfonate by uv irradiation in the presence of ethylenediaminetetraacetic acid, Chem. Eng. J. 379 (2020), 122338.
[52] C.G. Silva, et al., Developing highly active photocatalysts: gold-loaded ZnO for solar phenol oxidation, J. Catal. 316 (2014) 182.
[53] L. Sun, et al., N Self-Doped ZnO derived from microwave hydrothermal synthesized zeolitic imidazolate framework-8 toward enhanced photocatalytic degradation of methylene blue, J. Colloid Interface Sci. 565 (2020) 142.
[54] O. Fónagy, E. Szabó-Bárdos, O. Horváth, 1,4-Benzoquinone and 1,4-hydroquinone based determination of electron and superoxide radical formed in heterogeneous photocatalytic systems, J. Photochem. Photobiol. A Chem. 407 (2021), 113057.
[55] S. Bedouhène, F. Moulti-Mati, M. Hurtado-Nedelec, P.-M.-C. Dang, J. El-Benna, Luminol-amplified chemiluminescence detects mainly superoxide anion produced by human neutrophils, Am J Blood Res 7 (2017) 41.
[56] N. Bisceglia, M. Gravino, D. Savatin, Luminol-based assay for detection of immunity elicitor-induced hydrogen peroxide production in arabidopsis thaliana leaves, Bio Protoc 5 (2015).
[57] E. Alzahrani, E. Alzahrani, Photodegradation of binary azo dyes using core-shell Fe 3 O 4 /SiO 2 /TiO 2 nanospheres open access, Am J Analyt Chem 8 (2017) 95.
[58] Y.D. Bodke, Photocatalytic degradation of toxic methyl red dye using silica nanoparticles synthesized from rice husk ash, J. Environ. Anal. Toxicol. 5 (2015) 336.
[59] K. Davis, R. Yarbrough, M. Froeschle, J. White, and H. Rathnayake, Band Gap Engineered Zinc Oxide Nanostructures via a Sol-Gel Synthesis of Solvent Driven Shape-Controlled Crystal Growth †, (2019).
[60] D. Y. Momodu, F. Barzegar, B. Abdulhakeem, J. Dangbegnon, T. Masikhwa, J. Madito, and N. Manyala, Simonkolleite-Graphene Foam Composites and Their Superior Electrochemical Performance, (n.d.).
[61] N. Padmavathy, R. Vijayaraghavan, Enhanced bioactivity of ZnO nanoparticles-an antimicrobial study, Sci. Technol. Adv. Mater 9 (2008).
[62] K.R. Raghupathi, R.T. Koodali, A.C. Manna, Size-dependent bacterial growth inhibition and mechanism of antibacterial activity of zinc oxide nanoparticles, Langmuir 27 (2011) 4020.
[63] B. Pan, M. Feng, T.J. McDonald, K. Manoli, C. Wang, C.H. Huang, V.K. Sharma, Enhanced ferrate(VI) oxidation of micropollutants in water by carbonaceous materials: elucidating surface functionality, Chem. Eng. J. 398 (2020), 125607.
[64] R. Muttaqin, R. Pratiwi, Ratnawati, E. L. Dewi, M. Ibadurrohman, and Slamet, Degradation of Methylene Blue-Ciprofloxacin and Hydrogen Production Simultaneously Using Combination of Electrocoagulation and Photocatalytic Process with Fe-TiNTAs, Int J Hydrogen Energy 47, 18272 (2022).
[65] L. Wu, Q. Xie, Y. Lv, Z. Zhang, Z. Wu, X. Liang, M. Lu, Y. Nie, Degradation of methylene blue by dielectric barrier discharge plasma coupled with activated carbon supported on polyurethane foam, RSC Adv. 9 (2019) 25967.
[66] B. Wang, B. Dong, M. Xu, C. Chi, C. Wang, Degradation of methylene blue using double-chamber dielectric barrier discharge reactor under different carrier gases, Chem. Eng. Sci. 168 (2017) 90.
[67] B. Pan, M. Feng, J. Qin, A.A. Dar, C. Wang, X. Ma, V.K. Sharma, Iron(V)/Iron(IV) species in graphitic carbon nitride-ferrate(vi)-visible light system: enhanced oxidation of micropollutants, Chem. Eng. J. 428 (2022), 132610.
[68] E. Bilgin Simsek, Ö. Tuna, Z. Balta, Construction of stable perovskite-Type LaFeO3 particles on polymeric resin with boosted photocatalytic fenton-like decaffeination under solar irradiation, Sep. Purif. Technol. 237 (2020), 116384.
[69] X. Hu, et al., Mechanisms underlying the photocatalytic degradation pathway of ciprofloxacin with heterogeneous TiO2, Chem. Eng. J. 380 (2020), 122366.
[70] M. Sarafraz, M. Sadeghi, A. Yazdanbakhsh, M.M. Amini, M. Sadani, A. Eslami, Enhanced photocatalytic degradation of ciprofloxacin by black Ti3+/N-TiO2 under visible LED light irradiation: kinetic energy consumption degradation pathway, and toxicity assessment, Process Safety Environ. Prot. 137 (2020) 261.
[71] T. Montalvo-Herrera, D. Sánchez-Martínez, D.B. Hernandez-Uresti, L.M. Torres-Martínez, The role of the reactive oxygen species and the influence of KBiO 3 synthesis method in the photodegradation of methylene blue and ciprofloxacinreaction kinetics, Mechanisms and Catalysis 126 (2019) 561.
[72] G. Ognibene, D. A. Cristaldi, R. Fiorenza, I. Blanco, G. Cicala, S. S. Scirè, and M. E. Fragalà, Photoactivity of Hierarchically Nanostructured ZnO-PES Fibre Mats for Water Treatments, (2016).
[73] X. Yu, J. Zhang, J. Zhang, J. Niu, J. Zhao, Y. Wei, B. Yao, Photocatalytic degradation of ciprofloxacin using Zn-doped Cu2O particles: analysis of degradation pathways and intermediates, Chem. Eng. J. 374 (2019) 316.
[74] O. Koysuren, H.N. Koysuren, Preparation and activity evaluation of B4C/ZnO composite photocatalyst, J Solgel Sci Technol 103 (2022) 172.
[75] P. Mikrut, A. Święs, M. Kobielusz, L. Chmielarz, and W. Macyk, Selective and Efficient Catalytic and Photocatalytic Oxidation of Diphenyl Sulphide to Sulfoxide and Sulfone: The Role of Hydrogen Peroxide and TiO2 Polymorph, RSC Adv **12**, 1862 (2022).